Since January 2020 Elsevier has created a COVID-19 resource centre with free information in English and Mandarin on the novel coronavirus COVID-19. The COVID-19 resource centre is hosted on Elsevier Connect, the company's public news and information website.

Computers in Biology and Medicine 134 (2021) 104453

Contents lists available at ScienceDirect

Computers in Biology and Medicine

journal homepage: www.elsevier.com/locate/compbiomed

LBP-based information assisted intelligent system for COVID-19 identification

Shishir Maheshwari [a], Rishi Raj Sharma [b,*], Mohit Kumar [c]

[a] Discipline of Electrical and Electronics Engineering, Birla Institute of Technology and Science, Pilani, 333031, India
[b] Department of Electronics Engineering, Defence Institute of Advanced Technology, Pune, 411025, India
[c] NAF Department, Indian Institute of Technology Kanpur, Kanpur, India

ARTICLE INFO

Keywords:
COVID-19
Local binary pattern
Entropy
Gray level co-occurrence matrix
Support vector machine classifier
Chest X-ray

ABSTRACT

A real-time COVID-19 detection system is an utmost requirement of the present situation. This article presents a chest X-ray image-based automated COVID-19 detection system which can be employed with the RT-PCR test to improve the diagnosis rate. In the proposed approach, the textural features are extracted from the chest X-ray images and local binary pattern (LBP) based images. Further, the image-based and LBP image-based features are jointly investigated. Thereafter, highly discriminatory features are provided to the classifier for developing an automated model for COVID-19 identification. The performance of the proposed approach is investigated over 2905 chest X-ray images of normal, pneumonia, and COVID-19 infected persons on various class combinations to analyze the robustness. The developed method achieves 97.97% accuracy (acc) and 99.88% sensitivity (sen) for classifying COVID-19 X-ray images against pneumonia infected and normal person's X-ray images. It attains 98.91% acc and 99.33% sen for COVID-19 X-ray against the normal X-ray classification. This method can be employed to assist the radiologists during mass screening for fast, accurate, and contact-free COVID-19 diagnosis.

1. Introduction

The Severe Acute Respiratory Syndrome (SARS) related viruses come under the coronavirus family [1]. A recently found coronavirus of this family is known as Severe Acute Respiratory Syndrome Coronavirus-2 (SARS-CoV-2). It becomes a pandemic disease termed as coronavirus infectious disease 2019 (COVID-19) [2]. It was originated due to an unknown cause in Wuhan city, province of China, at the end of 2019 and spread rapidly throughout the globe [3,4]. The primary diagnosis method for COVID-19 is a real-time reverse transcription-polymerase chain reaction (RT-PCR), which is widely used throughout the world. In the RT-PCR test, the complementary DNA (cDNA) is obtained using the reverse transcriptase process. After that, the PCR process is performed in three steps namely, denaturation, annealing, and elongation [5]. The COVID-19 disease is highly transmissible due to direct-indirect association in the social circle and long duration sustainability of virus on different objects. Mostly, the SARS-COV-2 virus enters in human-body through the nose and mouth and retains there, which increases the viral load rapidly. Due to continuous respiration, it reaches the lungs and affects the respiration process. Therefore, symptoms can be observed in lungs [6]. The chest X-ray and computed tomography (CT) scan-based radiological imaging methods are extensive factors in early diagnosis [7].

The deep neural network model CoroNet is proposed for classifying pneumonia, COVID-19, and normal cases with 89.6% accuracy [8]. Another deep neural network model COVID-Net is designed in [9] and other methods are also proposed [10]. Some researchers have used the ultrasound technique to monitor the COVID-19 positive patients [11]. The chest CT scans are used for ensemble support vector machine-based model development for COVID-19 detection [12]. Another CT image-based methodology for COVID-19 detection is developed using a deep network in which segmentation is applied to select the infected lungs region [13]. The texture descriptor of chest X-ray image based COVID-19 identification method is presented with 0.8889 F_1 score in [14]. Recently, a fusion of multiple classifiers based method is developed for COVID-19 detection using X-ray images [15]. An autoregressive-moving-average based COVID-19 cases prediction method is developed in [16].

* Corresponding author.
E-mail addresses: shishir.maheshwari@pilani.bits-pilani.ac.in (S. Maheshwari), dr.rrsrrs@gmail.com, rsharma@diat.ac.in (R.R. Sharma), er09mohit@gmail.com (M. Kumar).

https://doi.org/10.1016/j.compbiomed.2021.104453
Received 27 February 2021; Received in revised form 19 April 2021; Accepted 24 April 2021
Available online 1 May 2021

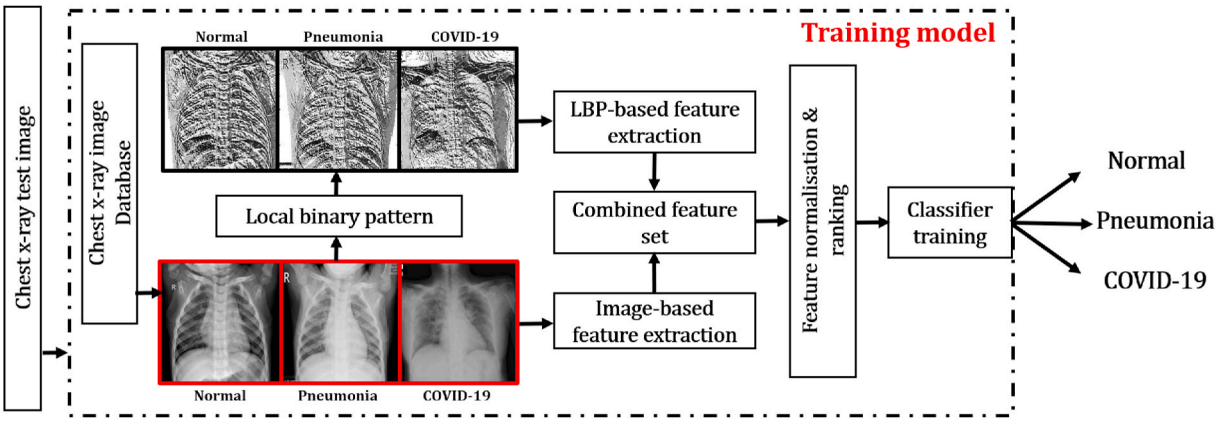

Fig. 1. Block diagram of the proposed approach.

1.1. Need of research

The diagnostic duration of the COVID-19 is a crucial factor as the viral load increases rapidly inside the human body. The RT-PCR test takes nearly four dedicated hours to detect the COVID-19. It increases up to 10–12 h as per the time taken in the sample collection and availability of the laboratory. The accessibility of the RT-PCR test and getting final results are the key parameters to begin the treatment. Therefore, a fast and accurate diagnosis for COVID-19 is of the utmost importance. The sensitivity of RT-PCR test is very low (nearly 65%) and high miss-detection is observed. However, the symptoms of COVID-19 are noticed in different radiological examinations [17,18]. Therefore, the radiological observations are crucial and can overcome the limitations of RT-PCR test [19]. The availability of radio images of COVID-19 patients, pneumonia patients, and healthy persons is highly unbalanced [20].

The process of X-ray imaging is very fast, contact-free, and easily available in most countries [21,22]. Therefore, an X-ray based highly accurate automated system with high sensitivity is needed to control the present COVID-19 pandemic. Most of the proposed models are based on neural network and deep learning, which require large size dataset to get good accuracy and sensitivity. Therefore, an X-ray image features based method is required to overcome the issue of large data availability, complete dependency on RT-PCR test, and time consuming CT scan process. Moreover, availability of X-ray imaging facilities are more in remote areas as compared to the CT scan. The X-ray process can be helpful in diagnosing and controlling of COVID-19 pandemic.

In this paper, an image texture-based features are investigated, and a method is proposed to distinguish X-ray images of SARS-COV-2 patients from normal persons and pneumonia patients. In the present work, texture-based features, various image-based entropy features, co-occurrence matrix, and local binary pattern [23] are studied extensively. Based on these features, a support vector machine (SVM) classifier is employed to design an automated method for COVID-19 detection with respect to normal and pneumonia patients. The suitable kernel features of SVM are selected to achieve high sensitivity and accuracy.

The rest of the paper is organized as follows. The proposed method for COVID-19 detection is detailed in Section-2. Section-3 describes the dataset and experimental setup. Results and discussion are explained in Section-4. Finally, the overall article is concluded in Section-5 with possible future work.

2. Approach for COVID-19 detection

The pictorial representation of the proposed approach is shown in Fig. 1. The proposed approach is developed for COVID-19 detection using chest X-ray images. The sample chest X-ray images are also shown in Fig. 1. In this method, first, the textural features are extracted from the chest X-ray images which are termed as image-based features. Second, the local binary patterns (LBPs) [23] of the chest X-ray images are obtained. The same set of features are extracted from LBPs and termed as LBP-based features. Further, these features are combined to obtain the combined feature set. Thereafter, the extracted features are normalized and ranked. Then, a subset of feature vector is selected from the ranked features. Finally, the support vector machine (SVM) classifier is employed for COVID-19 detection.

2.1. Local binary pattern (LBP)

The LBP [24] is computed from the chest X-ray image which is an effective texture descriptor. It incorporates the local pixel intensities information in a binary coded decimal value. The LBP [24] is computed from the chest X-ray image which is an effective texture descriptor. It incorporates the local pixel intensities information in a binary coded decimal value. It has been widely used in texture-based applications as it characterizes the local variation in gray levels [23].

2.2. Features

The gray-level co-occurrence matrix (GLCM), entropy-based features, zernike phase and amplitude, Hu's moments, and fractal dimension (FD) are computed from chest X-ray and its LBP-images. These are briefly explained in section below.

2.2.1. GLCM features

It is a statistical method to examine the texture by considering the spatial relationship of pixels. Its elements are created by the relative number of times the gray level pair (c, d) occurs when pixels are separated by the distance (c, d) = (1, 0). For a m × n image, it can be defined as [25,26]:

$$G_d(j,k) = |(c,d),(c+x,d+y) : I(c,d) = j, I(c+x,d+y) = k| \quad (1)$$

The 29 textural features are extracted from the obtained GLCM of the chest X-ray image [26].

2.2.2. Entropy based features

The entropy-based features are also employed to measure the subtle variation in the textures. Three different entropy-based measures, namely Renyi entropy (RE), Yager entropy (YE), and Kapur entropy (KE), are utilized in the present work.

RE is defined as [27]

$$RE = \frac{1}{1-A} log_2 \sum_{j=0}^{g-1} h_j^A \quad (2)$$

where $A \neq 1$, and A > 0. The RE is a concentration measure parameter. It

is also used to measure the concentration of time-frequency images [28,29].

YE can be defined as [30]

$$YE = 1 - \frac{\sum_{j=0}^{g-1} |2h_i - 1|}{|P \times Q|} \tag{3}$$

where $P \times Q$ denotes the size of image.

KE is defined as [27]

$$KE = \frac{1}{B-A} log_2 \frac{\sum_{j=0}^{g-1} h_j^A}{\sum_{j=0}^{g-1} h_j^B} \tag{4}$$

where A≠ B, and A, B > 0. Where g is number of gray levels of image. These entropy based features are widely applied for the analysis of images in the different applications such as glaucoma diagnosis in [23] and for the analysis of retinal health in [31]. These entropies have been previously found to be effective for human seizure detection [32,33], identification of focal Electroencephalogram (EEG) signals [34], and characterization of fatty liver disease [35]. The advantage of these entropies lies in their generality and flexibility due to the parameters involved, which enable several measurements of uncertainty [23].

2.2.3. Zernike moments

It is a projection of an image function on to the orthogonal basis functions named as Zernike polynomials. For an order p and repetition q, it can be defined as [36,37]:

$$A_{pq} = \frac{p+1}{\pi} \int\int f(x,y) \left[V_{pq}(x,y)\right]^* dxdy \tag{5}$$

where, $x^2 + y^2 \leq 1$ and $V_{pq}(x,y)$ is the Zernike polynomials which is defined in [36,37]. This provides two features namely Zernike amplitude and Zernike phase.

2.2.4. Hu's moments

The Hu's moment represents the invariant image patterns. The Hu's moments for an image f(x,y) can be given as [38,39]:

$$H_{m,n} = \sum_x \sum_y x^m y^n f(x,y) \tag{6}$$

The central moments for non negative values of m and n can be defined as [39]:

$$\mu_{m,n} = \sum_x \sum_y (x - \bar{x})^m (y - \bar{y})^n f(x,y) \tag{7}$$

where, $\bar{x} = \frac{H_{10}}{H_{00}}$ and $\bar{y} = \frac{H_{01}}{H_{00}}$. Therefore, the normalized central moments can be denoted as:

$$\partial_{m,n} = \frac{\mu_{mn}}{\mu^{\tau}_{00}} \quad for \;\; m,n = 0,1,2,3....., \tag{8}$$

where, $\tau = (m+n)/2 + 1$.

Now, the 7 Hu's moments, denoted as $HM_1 - HM_7$, can be extracted which are explained in [38,39]. These moments are used as features for the detection of liver's fibrosis stages in [39].

2.2.5. Fractal dimension

It is based on the concept of the self similarity. It has a property of scale dependence which is useful for analysing the textures. It is used in Ref. [23] to capture the texture difference between glaucoma and normal images and can be defined as [40]:

$$d = \frac{logM_r}{log(1/r)}. \tag{9}$$

A texture is said to be self-similar if it is a union of M_r. Where, M_r are the distinct copies of a texture at a scale up or down by a factor r [40]. It shows higher values if the roughness of the texture is high [26].

Table 1
Ranked image-based features of Normal vs COVID-19 class.

Feature	Normal	COVID-19 (%)
	mn ± sd	mn ± sd (%)
Fractal dimension	2.24 ± .019	2.18 ± .03
Hu moment 2	16.58 ± 0.90	19.06 ± 2.13
Zernike amplitude	6.52 ± 3.24	12.62 ± 7.48
Zernike Phase	−98.32 ± 81.04	−20.54 ± 63.08
Long run low gray level run emphasis	1.34 ± 1.66	3.04 ± 3.90
Variance	3767.95 ± 684.66	2879.38 ± 1298.63
Kurtosis	2.35 ± 0.36	269 ± 0.84
Low gray level run emphasis	0.07 ± 0.05	0.12 ± 0.11
Hu moment 1	6.72 ± 0.09	6.73 ± 0.19
Renyi entropy	5.63 ± 1.00	6.23 ± 1.23

*mn = mean, sd = standard deviation.

Table 2
Ranked LBP-based features of Normal vs COVID-19 class.

Feature	Normal	COVID-19 (%)
	mn ± sd	mn ± sd (%)
Zernike phase	−16.82 ± 36.48	−7.33 ± 73.70
Hu moment 2	19.14 ± 0.981	20.03 ± 1.41
Skewness	−0.14 ± 0.080	−0.10 ± 0.17
Hu monent 1	6.68 ± 0.023	6.69 ± 0.06
Hu moment 4	27.18 ± 0.77	27.58 ± 1.54
Fractal dimension	2.61 ± 0.009	2.61 ± 0.02
Variance	7679.63 ± 302.97	7647.63 ± 483.51
Hu moment 3	26.01 ± 1.03	26.53 ± 1.30
Renyi entropy	4.47 ± 0.476	4.54 ± 0.75
Hu moment 7	54.61 ± 1.57	55.48 ± 2.66

2.3. Feature normalisation and selection

In this work, zero mean and unit standard deviation [41] is employed to normalize the extracted features. In the performance evaluation, all features do not provide the same discrimination capability. Therefore, the subset of features is selected from the normalized features. In the proposed work, we have employed ReliefF [42] feature selection method. Tables 1 and 2 tabulates first 10 features after feature selection.

2.4. Support vector machine (SVM)

The SVM classifier [43–45] is employed for classification with radial basis function (RBF) [46] as a kernel. Let there be D data points $\{i_n, c_n\}_{n=1}^{D}$, where $i_n \in \mathbb{R}^m$ and $c_n \in \mathbb{R}^m$ are n^{th} input data sample and corresponding class label, respectively. Further, the SVM classifier can be formulated as [47]:

$$P(i) = \text{sign}\left[\sum_{n=1}^{D} \mathbf{a}_n c_n \mathbf{K}(i, i_n) + \mathbf{b}\right] \tag{10}$$

where $\mathbf{a}_n$ positive real constant, $\mathbf{K}(i, i_n)$ is a kernel function and $\mathbf{b}$ is a real constant.

In 10, $\mathbf{K}(i, i_n)$ is the RBF kernel function which is expressed as [47]:

$$\mathbf{K}(i, i_n) = \exp\left[\frac{-||i - i_n||^2}{2\sigma^2}\right] \tag{11}$$

The kernel parameter, σ, is varied from 0.5 to 3 with a step size of

0.1. The performance of the proposed approach is validated using 3-fold cross-validation [48]. Accuracy and sensitivity [49] are utilized as a measure of performance.

3. Dataset & experimental setup

3.1. Dataset

The dataset utilized in this work is obtained from Kaggle. It consists of chest X-ray images of 3 classes which are normal, pneumonia, and COVID-19 infected persons. All the images are in 1024 × 1024 resolution stored in portable network graphics (PNG) file format. There are 2905 X-ray images, of which 1341, 1345, and 219 images belong to normal persons, pneumonia-infected patients, and COVID-19 infected patients, respectively.

3.2. Experimental setup

To evaluate the performance of the proposed approach, the following experimental setup has been adopted in this paper:

3.2.1. Based on the features

In the proposed approach, the features are extracted from the chest X-ray images in the following three ways, such as:

1 Image-based features: The features are directly extracted from the chest X-ray images.
2 LBP-based features: The LBPs are obtained from the chest X-ray images. Thereafter, the features are extracted from the LBPs.
3 Combined features: The image-based and LBP-based features are combined to perform the experiments.

3.2.2. Based on the class

The database used in this work consists of three classes. To evaluate the performance of the proposed approach, the experimental set-up is organised as follows:

1 One-vs-One (OvO): In this experimental setup, binary classification is performed between the extracted features of any two classes while discarding the third class. For convention, normal class versus (vs) COVID-19 class, normal class vs Pneumonia class, and Pneumonia class vs COVID-19 class is denoted as N vs C, N vs P, and P vs C, respectively.
2 One-vs-All (OvA): In this experimental setup, the extracted features of any two classes are combined and treated as a single class. Thereafter, the binary classification is performed between the combined and remaining classes. Similar to OvO convention, the OvA classes are categorized as normal plus COVID-19 vs Pneumonia (NC vs P), normal plus Pneumonia vs COVID-19 (NP vs C), and normal vs Pneumonia plus COVID-19 (N vs PC).

4. Results & discussion

Potency of the proposed method is examined based on features for different class combinations. The number of features extracted from a single chest X-ray image via the image-based method, LBP-based method, and combined method are 42, 42, and 84, respectively. Thereafter, the subset of features is selected from the original feature vector by employing the feature selection method. In the proposed method, first 25 features are selected from the ranked original feature vector using the ReliefF feature selection method. Further, in the proposed approach, the ranked feature vector is fed to the SVM classifier for classification. The ranked image-based and LBP-based features for N vs C have been tabulated in Tables 1 and 2, respectively. From these tables, it is perceived that fractal dimension, Zernike amplitude, Zernike phase, Hu moment 2, and Renyi entropy are highly discriminatory as well as highly prioritized using ReliefF-based feature ranking method. Therefore, these features may contribute significantly to distinguish the COVID-19 class from other classes.

Table 3
Classification performance for One-vs-One (OvO) experimental setup.

Type	Class	acc (%)	sen (%)
Image-based features	N vs C	99.04	99.55
	N vs P	92.60	95.07
	P vs C	97.57	99.47
LBP image-based features	N vs C	96.99	98.90
	N vs P	92.44	94.18
	P vs C	95.14	98.66
Combined features	N vs C	98.91	99.33
	N vs P	94.19	94.55
	P vs C	97.89	99.70

*acc = accuracy, sen = sensitivity, N = Normal class, P = Pneumonia class, C = COVID-19 class.

4.1. Effect of LBP on information enhancement

The use of features computed from LBP based images along with the features extracted from X-ray images enhances the texture-based information. Various features explained in section 2.2 are computed from LBPs of X-ray images. From Tables 1 and 2, it can be observed that FD computed from the LBPs of image has shown higher values as compared to the FD computed from the image without LBP. A higher mean value of FD indicates higher roughness of the texture. Hence, LBP is useful to increase the roughness of the texture which in turn improves the feature discrimination. Moreover, FD computed from the LBPs of image has shown lower values of standard deviation than FD computed from an image without LBP.

It can also be interpreted from Tables 1 and 2 that the RE computed from the LBP images is found lesser then the RE computed from X-ray images. Higher values of RE are an indication of a higher concentration of information in the textures. After applying the ReliefF based feature ranking method, it is observed that Renyi has achieved 9th position out of 42 features in LBP image based features while other entropy features are ranked lower position. Hence, RE computed from the LBP image show a lower concentration of information than RE computed without LBP. However, the standard deviation for RE computed from the LBP image is found lower than the direct computation of RE from the images.

The Hu moment-based features are applied for pattern recognition. The shape-related information in terms of spatial and intensity patterns is associated with the order of Hu moment. In Tables 1 and 2, it can be observed that the Hu moment 2 achieves a higher rank in both image-based features and LBP-based features for normal vs COVID-19 class. The mean values of Hu moment 2 are high for the LBP image as compared to the image-based computation. Moreover, the deviation is also high for the Hu moment 2 feature computed directly over the X-ray image than computed over the LBP-based X-ray image. In this way, it can be said that the LBP-based features are useful and can be applied to improve the distinguish behavior of the proposed methodology for COVID-19 identification.

4.2. Experimental results

Experimental results obtained for the proposed approach for different combination of classes are tabulated in Table 3 for experimental setup-1, i.e., OvO. The proposed approach achieves the classification acc of 99.04%, 92.60%, and 97.57% and sen of 99.55%, 95.07%, and 99.47% for N vs C, N vs P and P vs C, respectively for image-based method. On the other hand, for the combined features, the proposed approach achieves classification acc of 98.91%, 94.19%, and 97.89% and sen of 99.33%, 94.55%, and 99.70% for N vs C, N vs P and P vs C, respectively. The proposed method achieves high acc and sen while sen

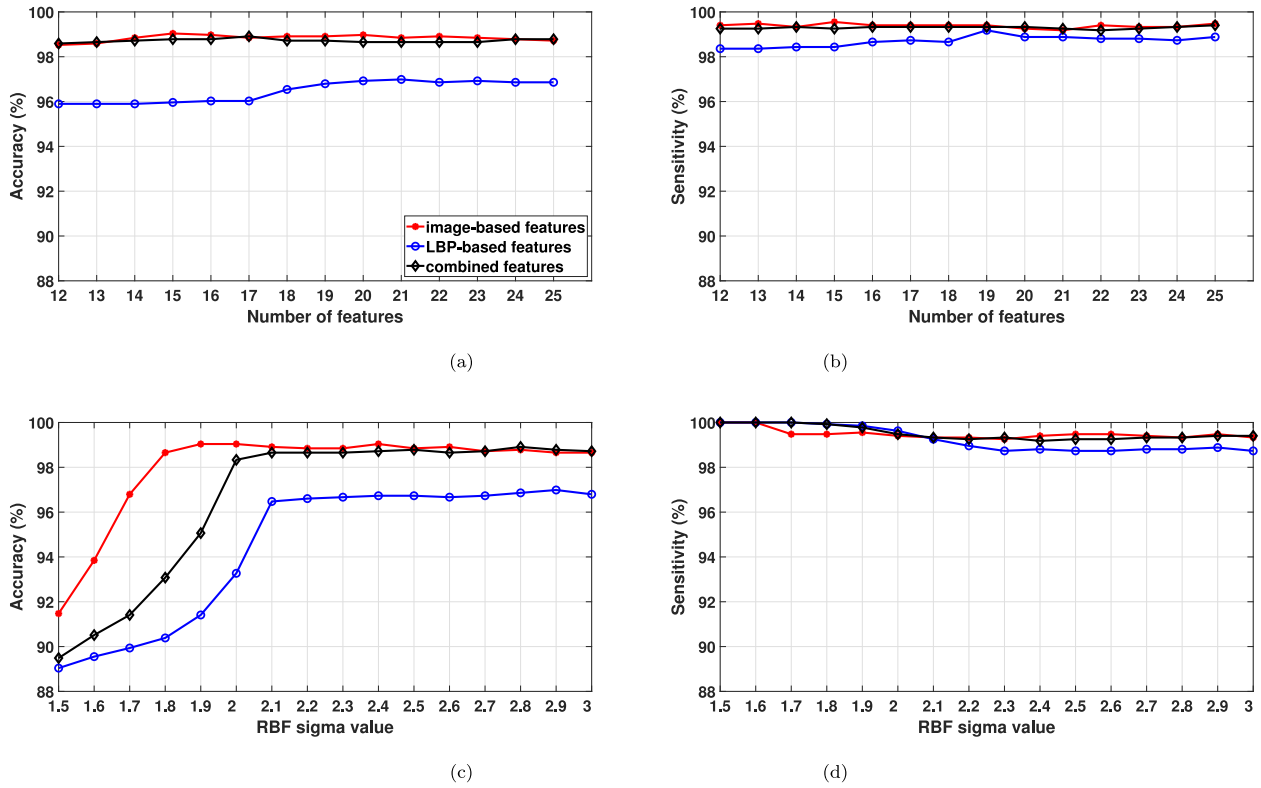

Fig. 2. Classification performance for N v C. (a) and (b) represent the plot of accuracy and sensitivity against the number of features for all three cases. (c) and (d) represents accuracy and sensitivity against the RBF sigma values.

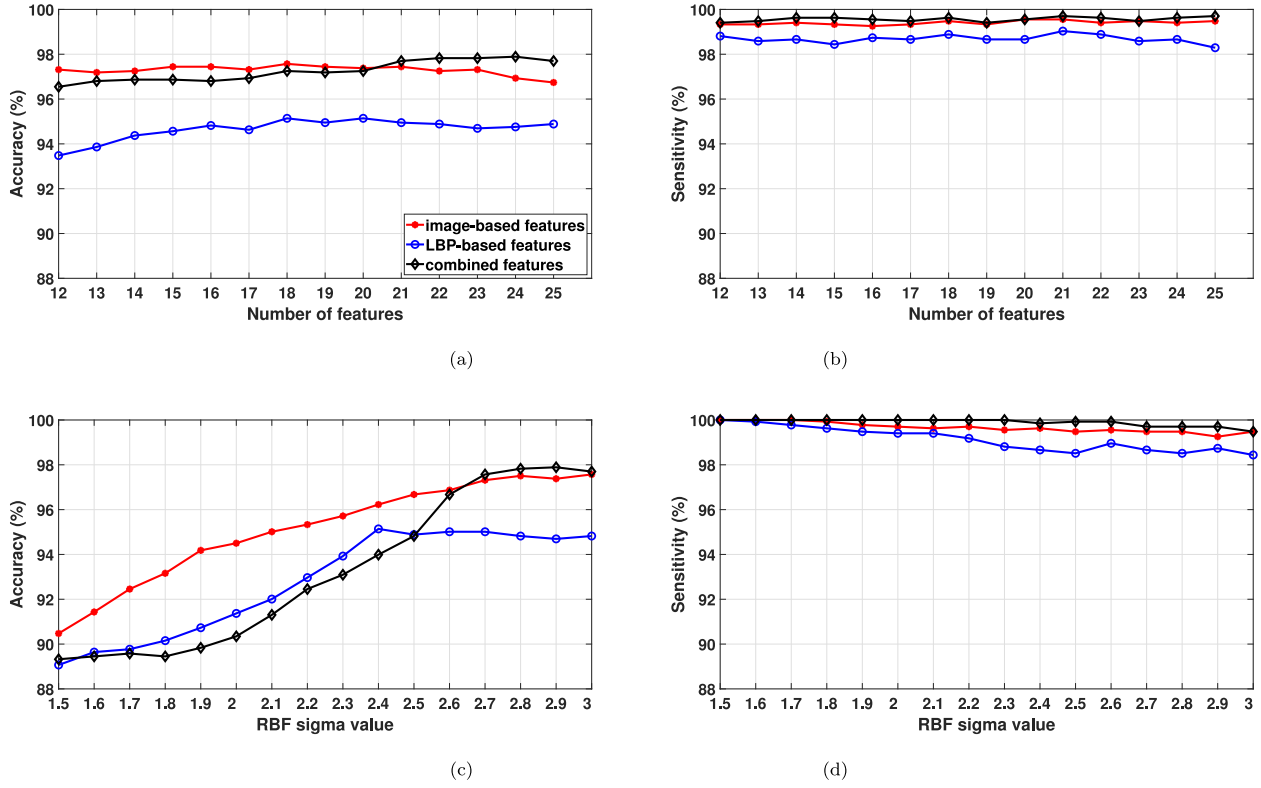

Fig. 3. Classification performance for P v C. (a) and (b) represent the plot of accuracy and sensitivity against the number of features for all three cases. (c) and (d) represents accuracy and sensitivity against the RBF sigma values.

Table 4
Classification performance for One-vs-All (OvA) experimental setup.

Type	Class	acc (%)	sen (%)
Image-based features	NC vs P	91.88	94.55
	NP vs C	98.11	99.70
	N vs PC	92.67	98.88
LBP image-based features	NC vs P	90.64	93.84
	NP vs C	96.54	99.66
	N vs PC	92.36	92.77
Combined features	NC vs P	93.32	94.55
	NP vs C	97.97	99.88
	N vs PC	93.94	93.88

of RT-PCR test is very less and showed miss-detections [18].

Fig. 2 represents the classification performance plot for N vs C experimental setup. The variation of acc and sen with respect to the number of features is shown in Fig. 2 (a) and (b), and it can be observed that the image-based features achieve the highest acc and sen using the first 15 features. The variation in the acc and sen with respect to the RBF sigma values can be observed in Fig. 2 (c) and (d). It can also be noticed that the RBF sigma value is best suited in the range of 1.7–2.0. For the RBF sigma value higher then 2.0, sen is reduced in all three combinations of feature sets. The plots for classification performance of P vs C are delineated in Fig. 3. For P vs C, the combined method achieves high acc and sen using 21 features. The RBF sigma value in the range 2.7–3 is best suited for getting high acc and sen.

Furthermore, the experiments have also been performed for OvA experimental setup. The classification performance for OvA is tabulated in Table 4. Fig. 4 shows the plot of the classification performance for NP vs C. It can be observed from Table 4 that the image-based method and combined method achieves the classification acc 98.11% and 97.97% & sen 99.70% and 99.88% for NP vs C, respectively. Both the methods require 13 to 16 features to attain high acc and sen. The RBF sigma value should be in the range of 2.6–3.0 for achieving high acc with a little lower sen nearly 99.8%.

From Tables 3 and 4, it can be observed that the combined features provide better classification performance as compared to LBP-based features and image based features. Sen is a crucial parameter for reducing the misidentification and controlling the spread of the COVID-19 pandemic. By observing the sen values from Tables 3 and 4, it can be concluded that the combined approach provides better classification performance for the detection of COVID-19 cases. Very high sensitivity values such as 99.33%, 99.70%, and 99.88% are obtained for N vs C, P vs C, and NP vs C, respectively for combined feature setup. We have also computed the 3-class performance of the proposed approach. For the OvO setup, the average performance is computed by averaging the N vs P, P vs C, and N vs C. Similarly, in the OvA setup, the average has been taken for NP vs C, NC vs P, and N vs PC. The proposed method achieves a 3-class average classification acc of 97% and 95.08% for OvO and OvA experimental setup, respectively.

The proposed approach has also been compared with other existing methods for COVID-19 detection and shown in Table 5. It can be noticed from the comparison table that the proposed approach achieves better classification performance than the existing compared methodologies. The convolution neural network-based COVID-19 detection method achieved acc 96.78% for the two-class problem and 94.72% for three class problem. The deep neural network is applied for COVID-19 detection and attained the 98.08% acc for COVID-19 vs normal class and 87.2% acc for COVID-19 vs others. These methods require the availability of a larger dataset of COVID-19 X-ray images, which may be a significant issue. Other compared methods have been proposed mostly for COVID-19 vs normal class. Accomplishment of the proposed approach can be stated as follows:

1 Method achieves very high sen as well as acc for COVID-19 detection.
2 Significantly better classification performances than the state-of-the-art methods developed for COVID-19 detection.

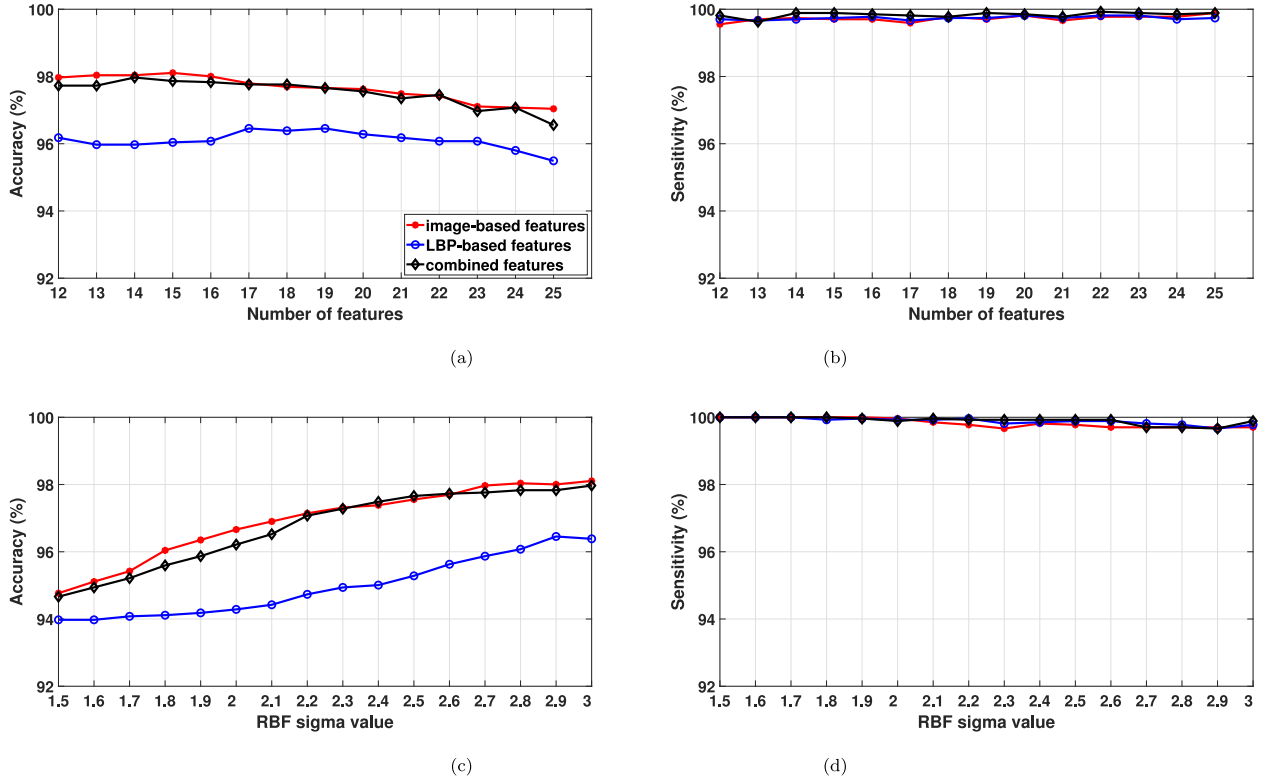

Fig. 4. Classification performance for NP v C. Fig. (a) and (b) represent the plot of accuracy and sensitivity against the number of features for all three cases. Fig. (c) and (d) represents accuracy and sensitivity against the RBF sigma values.

Table 5
A comparative summary of the existing methods for automated COVID-19 detection.

Author	No. of images	Image type	Method	Performance parameters (%)
Ioannis et al. [10]	C: 224, P: 700, N: 504	X-ray	VGG-19	acc: 93.48, sen: 92.85 (3-class) acc: 98.75, sen: 92.85 (2-class)
Sethy et al. [50]	C: 25, P: 25	X-ray	ResNet50 + SVM	acc: 95.38, sen: 97.30 (2-class)
Hemdan et al. [51]	C: 25, N: 25	X-ray	COVIDX-Net	acc: 90, sen: 90 (2-class)
Narin et al. [52]	C: 50, P: 50	X-ray	ResNet-50	acc: 98, sen: 96 (2-class)
Ying et al. [53]	C: 777, N: 708	CT-scan	DRE-Net	acc: 94, sen: 96 (2-class)
Wang et al. [54]	C: 195, P: 258	CT-scan	M-inception	acc: 82.90, sen: 83 (2-class)
Zheng et al. [55]	C: 313, P: 229	CT-scan	Unet	acc: 90.80, sen: 84 (2-class)
Xu et al. [56]	C: 219, P: 224, N: 175	CT-scan	ResNet	acc: 86.70, sen: NR (3-class)
Oztruk et al. [18]	C: 125, P: 500, N: 500	X-ray	DarkCovidNet	acc: 87.02, sen: 85.35 (3-class) acc: 98.08, sen: 95.13 (2-class)
Singh et al. [12]	C: 344, N: 358	CT-scan	Ensemble vector machine	acc: 95.7, sen: - (2-class)
Proposed approach	C: 219, P: 1345, N: 1341	X-ray	texture features	acc: 97, sen: 97.86 (3-class) acc: 97.97, sen: 99.88 (2-class, NP vs C) acc: 98.91, sen: 99.33 (2-class, N vs C)

*N = Normal class, P = Pneumonia class, C = COVID-19 class, ac = accuracy, sn = sensitivity, NR = not reported.

3 Provides better classification performances for both binary and three class cases.
4 A short range of RBF sigma values are suggested for faster and accurate detection.

In accordance with the above discussion, it can be stated that the present method highly appropriate for COVID-19 detection using chest X-ray images. In the future, the method will be tested using a larger size dataset considering other lung diseases, which may help the physicians to improve the accuracy of diagnosis.

5. Conclusion

In this article, a novel method for COVID-19 detection is introduced, which uses texture and LBP-based features. The present method is focused on the automated diagnosis of COVID-19 using entropy, co-occurrence matrix, fractal dimension, and LBP-based features. It reduces the dependency on the larger-size dataset as required in deep learning-based methods. In the proposed method, high sen is achieved with high acc for COVID-19 vs others (sen: 99.88%, acc: 97.97%), COVID-19 vs normal (sen: 99.33%, acc: 98.91%), and COVID-19 vs pneumonia (sen: 99.70%, acc: 97.89%) cases. It is evidenced that the Zernike amplitude & phase, Fractal dimension, Hu's moment are the key features that contributed remarkably for COVID-19 detection in all the considered experimental set-up. The proposed diagnostic system is contact-free, fast, and highly accurate. Therefore, it can be implemented in hospitals to assist the subject experts in the screening of COVID-19 patients. However, the data used in the study is not balanced as COVID-19 infected persons images are less. Study on large dataset is required. In the future, a cloud-based platform can be developed for COVID-19 detection in which the X-ray images can be uploaded from remote locations and fast results can be declared accurately. Moreover, the SARS-COV-2 virus load based study can be performed for infection severity level detection.

References

[1] J.F.-W. Chan, S. Yuan, K.-H. Kok, K.K.-W. To, H. Chu, J. Yang, F. Xing, J. Liu, C.C.-Y. Yip, R.W.-S. Poon, et al., A familial cluster of pneumonia associated with the 2019 novel coronavirus indicating person-to-person transmission: a study of a family cluster, Lancet 395 (2020) 514–523.
[2] F. Wu, S. Zhao, B. Yu, Y.-M. Chen, W. Wang, Z.-G. Song, Y. Hu, Z.-W. Tao, J.-H. Tian, Y.-Y. Pei, et al., A new coronavirus associated with human respiratory disease in China, Nature 579 (2020) 265–269.
[3] C. Huang, Y. Wang, X. Li, L. Ren, J. Zhao, Y. Hu, L. Zhang, G. Fan, J. Xu, X. Gu, et al., Clinical features of patients infected with 2019 novel coronavirus in wuhan, China, Lancet 395 (2020) 497–506.
[4] S. Latif, M. Usman, S. Manzoor, W. Iqbal, J. Qadir, G. Tyson, I. Castro, A. Razi, M.N. K. Boulos, A. Weller, J. Crowcroft, Leveraging data science to combat COVID-19: a comprehensive review, IEEE Trans. Artif. Intell. 1 (2020) 85–103.
[5] K. Yu, K. Pauls, Optimization of the PCR program for RAPD analysis, Nucleic Acids Res. 20 (1992) 2606.
[6] W.-j. Guan, Z.-y. Ni, Y. Hu, W.-h. Liang, C.-q. Ou, J.-x. He, L. Liu, H. Shan, C.-l. Lei, D.S. Hui, et al., Clinical characteristics of coronavirus disease 2019 in China, N. Engl. J. Med. 382 (2020) 1708–1720.
[7] Z.Y. Zu, M.D. Jiang, P.P. Xu, W. Chen, Q.Q. Ni, G.M. Lu, L.J. Zhang, Coronavirus disease 2019 (COVID): a perspective from China, Radiology (2020) 200490.
[8] A.I. Khan, J.L. Shah, M.M. Bhat, Coronet: a deep neural network for detection and diagnosis of COVID-19 from chest x-ray images, Comput. Methods Progr. Biomed. 196 (2020) 105581.
[9] L. Wang, Z.Q. Lin, A. Wong, COVID-net: a tailored deep convolutional neural network design for detection of COVID-19 cases from chest x-ray images, Sci. Rep. 10 (2020) 19549.
[10] I.D. Apostolopoulos, T.A. Mpesiana, COVID-19: automatic detection from x-ray images utilizing transfer learning with convolutional neural networks, Phys. Eng. Sci. Med. 43 (2020) 635–640.
[11] X. Qian, R. Wodnicki, H. Kang, J. Zhang, H. Tchelepi, Q. Zhou, Current ultrasound technologies and instrumentation in the assessment and monitoring of COVID-19 positive patients, IEEE Trans. Ultrason. Ferroelectrics Freq. Contr. 67 (2020) 2230–2240.
[12] M. Singh, S. Bansal, S. Ahuja, R. K. Dubey, B. K. Panigrahi, N. Dey, Transfer Learning Based Ensemble Support Vector Machine Model for Automated COVID-19 Detection Using Lung Computerized Tomography Scan Data, Medical & Biological Engineering & Computing.
[13] D.-P. Fan, T. Zhou, G.-P. Ji, Y. Zhou, G. Chen, H. Fu, J. Shen, L. Shao, Inf-net: automatic COVID-19 lung infection segmentation from CT images, IEEE Trans. Med. Imag. 39 (2020) 2626–2637.
[14] R.M. Pereira, D. Bertolini, L.O. Teixeira, C.N. Silla Jr., Y.M. Costa, COVID-19 identification in chest x-ray images on flat and hierarchical classification scenarios, Comput. Methods Progr. Biomed. 194 (2020) 105532.
[15] D. Sharifrazi, R. Alizadehsani, M. Roshanzamir, J.H. Joloudari, A. Shoeibi, M. Jafari, S. Hussain, Z.A. Sani, F. Hasanzadeh, F. Khozeimeh, et al., Fusion of convolution neural network, support vector machine and sobel filter for accurate detection of COVID-19 patients using X-ray images, Biomed. Signal Process Contr. 68 (2021) 102622.
[16] R.R. Sharma, M. Kumar, S. Maheshwari, K.P. Ray, EVDHM-ARIMA-based time series forecasting model and its application for COVID-19 cases, IEEE Trans. Instr. Meas. 70 (2020) 1–10.
[17] X. Xie, Z. Zhong, W. Zhao, C. Zheng, F. Wang, J. Liu, Chest CT for Typical 2019-nCoV Pneumonia: Relationship to Negative RT-PCR Testing, 2020, p. 200343. Radiology.
[18] T. Ozturk, M. Talo, E.A. Yildirim, U.B. Baloglu, O. Yildirim, U.R. Acharya, Automated detection of COVID-19 cases using deep neural networks with x-ray images, Comput. Biol. Med. 121 (2020) 103792.
[19] G.D. Rubin, C.J. Ryerson, L.B. Haramati, N. Sverzellati, J.P. Kanne, S. Raoof, N. W. Schluger, A. Volpi, J.-J. Yim, I.B. Martin, et al., The role of chest imaging in patient management during the COVID-19 pandemic: a multinational consensus statement from the fleischner society, Radiology 296 (2020) 172–180.
[20] J. Bridge, Y. Meng, Y. Zhao, Y. Du, M. Zhao, R. Sun, Y. Zheng, Introducing the GEV activation function for highly unbalanced data to develop COVID-19 diagnostic models, IEEE J. Biomed. Health Inf. 24 (2020) 2776–2786.
[21] F. Shi, J. Wang, J. Shi, Z. Wu, Q. Wang, Z. Tang, K. He, Y. Shi, D. Shen, Review of artificial intelligence techniques in imaging data acquisition, segmentation and diagnosis for COVID-19, IEEE Rev. Biomed. Eng. 14 (2021) 4–15.
[22] M.E. Chowdhury, T. Rahman, A. Khandakar, R. Mazhar, M.A. Kadir, Z.B. Mahbub, K.R. Islam, M.S. Khan, A. Iqbal, N. Al-Emadi, et al., Can ai help in screening viral and COVID-19 pneumonia? IEEE Access 8 (2020) 132665–132676.
[23] S. Maheshwari, V. Kanhangad, R.B. Pachori, S.V. Bhandary, U.R. Acharya, Automated glaucoma diagnosis using bit-plane slicing and local binary pattern techniques, Comput. Biol. Med. 105 (2019) 72–80.
[24] T. Ojala, M. Pietikainen, T. Maenpaa, Multiresolution gray-scale and rotation invariant texture classification with local binary patterns, IEEE Trans. Pattern Anal. Mach. Intell. 24 (2002) 971–987.

[25] R.M. Haralick, K. Shanmugam, I. Dinstein, Textural features for image classification, IEEE Trans. Syst. Man Cybern. SMC- 3 (1973) 610–621.
[26] U.R. Acharya, S.V. Sree, L. Saba, F. Molinari, S. Guerriero, J.S. Suri, Ovarian tumor characterization and classification using ultrasound—a new online paradigm, J. Digit. Imag. 26 (2013) 544–553.
[27] M. Mookiah, U.R. Acharya, R.J. Martis, C.K. Chua, C. Lim, E. Ng, A. Laude, Evolutionary algorithm based classifier parameter tuning for automatic diabetic retinopathy grading: a hybrid feature extraction approach, Knowl. Base Syst. 39 (2013) 9–22.
[28] L. Stanković, A measure of some time-frequency distributions concentration, Signal Process. 81 (2001) 621–631.
[29] R. Panda, S. Jain, R. Tripathy, R.R. Sharma, R.B. Pachori, Sliding mode singular spectrum analysis for the elimination of cross-terms in Wigner-Ville distribution, Circ. Syst. Signal Process. 40 (2021) 1207–1232.
[30] M.R.K. Mookiah, U.R. Acharya, J.E. Koh, V. Chandran, C.K. Chua, J.H. Tan, C. M. Lim, E. Ng, K. Noronha, L. Tong, A. Laude, Automated diagnosis of age-related macular degeneration using greyscale features from digital fundus images, Comput. Biol. Med. 53 (2014) 55–64.
[31] U.R. Acharya, M.R.K. Mookiah, J.E. Koh, J.H. Tan, S.V. Bhandary, A.K. Rao, H. Fujita, Y. Hagiwara, C.K. Chua, A. Laude, Automated screening system for retinal health using bi-dimensional empirical mode decomposition and integrated index, Comput. Biol. Med. 75 (2016) 54–62.
[32] A. Feltane, G.F.B. Bartels, J. Gaitanis, Y. Boudria, W. Besio, Human seizure detection using quadratic rényi entropy, in: 2013 6th International IEEE/EMBS Conference on Neural Engineering, NER), 2013, pp. 815–818.
[33] R.R. Sharma, R.B. Pachori, Time-frequency representation using IEVDHM-HT with application to classification of epileptic EEG signals, IET Sci. Meas. Technol. 12 (2017) 72–82.
[34] R. Sharma, R.B. Pachori, U.R. Acharya, Application of entropy measures on intrinsic mode functions for the automated identification of focal electroencephalogram signals, Entropy 17 (2015) 669–691.
[35] U.R. Acharya, U. Raghavendra, H. Fujita, Y. Hagiwara, J.E. Koh, T.J. Hong, V. K. Sudarshan, A. Vijayananthan, C.H. Yeong, A. Gudigar, K.H. Ng, Automated characterization of fatty liver disease and cirrhosis using curvelet transform and entropy features extracted from ultrasound images, Comput. Biol. Med. 79 (2016) 250–258.
[36] A. Tahmasbi, F. Saki, S.B. Shokouhi, Classification of benign and malignant masses based on zernike moments, Comput. Biol. Med. 41 (2011) 726–735.
[37] C. Teh, R.T. Chin, On image analysis by the methods of moments, IEEE Trans. Pattern Anal. Mach. Intell. 10 (1988) 496–513.
[38] Ming-Kuei Hu, Visual pattern recognition by moment invariants, IRE Trans. Inf. Theor. 8 (1962) 179–187.
[39] U.R. Acharya, U. Raghavendra, J.E.W. Koh, K.M. Meiburger, E.J. Ciaccio, Y. Hagiwara, F. Molinari, W.L. Leong, A. Vijayananthan, N.A. Yaakup, M.K.B. M. Fabell, C.H. Yeong, Automated detection and classification of liver fibrosis stages using contourlet transform and nonlinear features, Comput. Methods Progr. Biomed. 166 (2018) 91–98.
[40] B.B. Chaudhuri, N. Sarkar, Texture segmentation using fractal dimension, IEEE Trans. Pattern Anal. Mach. Intell. 17 (1995) 72–77.
[41] M.H. Dunham, Data Mining: Introductory and Advanced Topics, Prentice Hall PTR, USA, 2002.
[42] I. Kononenko, Estimating attributes: analysis and extensions of relief, in: European Conference on Machine Learning, 1994, pp. 171–182.
[43] C.J. Burges, A tutorial on support vector machines for pattern recognition, Data Min. Knowl. Discov. 2 (1998) 121–167.
[44] S. Maheshwari, R.B. Pachori, V. Kanhangad, S.V. Bhandary, U.R. Acharya, Iterative variational mode decomposition based automated detection of glaucoma using fundus images, Comput. Biol. Med. 88 (2017) 142–149.
[45] S. Maheshwari, R.B. Pachori, U.R. Acharya, Automated diagnosis of glaucoma using empirical wavelet transform and correntropy features extracted from fundus images, IEEE J. Biomed. Health Inf. 21 (2017) 803–813.
[46] A.H. Khandoker, D.T.H. Lai, R.K. Begg, M. Palaniswami, Wavelet based feature extraction for support vector machines for screening balance impairments in the elderly, IEEE Trans. Neural Syst. Rehabil. Eng. 15 (2007) 587–597.
[47] J.A.K. Suykens, J. Vandewalle, Least squares support vector machine classifiers, Neural Process. Lett. 9 (1999) 293–300.
[48] R. Kohavi, A study of cross-validation and bootstrap for accuracy estimation and model selection, in: International Joint Conference on Artificial Intelligence, vol. 14, 1995, pp. 1137–1145.
[49] A.T. Azar, S.A. El-Said, Performance analysis of support vector machines classifiers in breast cancer mammography recognition, Neural Comput. Appl. 24 (2014) 1163–1177.
[50] P. Sethy, S. Behera, Detection of Coronavirus Disease (COVID-19) Based on Deep Features, Preprints.
[51] E.E.-D. Hemdan, M.A. Shouman, M.E. Karar, COVIDx-Net: a Framework of Deep Learning Classifiers to Diagnose COVID-19 in X-Ray Images, 2003, p. 11055, arXiv preprint arXiv.
[52] A. Narin, C. Kaya, Z. Pamuk, Automatic Detection of Coronavirus Disease (COVID-19) Using X-Ray Images and Deep Convolutional Neural Networks, 2003, p. 10849, arXiv preprint arXiv.
[53] Y. Song, S. Zheng, L. Li, X. Zhang, X. Zhang, Z. Huang, J. Chen, R. Wang, H. Zhao, Y. Zha, J. Shen, Y. Chong, Y. Yang, Deep learning enables accurate diagnosis of novel coronavirus (COVID-19) with CT images, IEEE ACM Trans. Comput. Biol. Bioinf. (2021), https://doi.org/10.1109/TCBB.2021.3065361.
[54] S. Wang, B. Kang, J. Ma, X. Zeng, M. Xiao, J. Guo, M. Cai, J. Yang, Y. Li, X. Meng, B. Xu, A deep learning algorithm using CT images to screen for corona virus disease (COVID-19), European Radiology.
[55] C. Zheng, X. Deng, Q. Fu, Q. Zhou, J. Feng, H. Ma, W. Liu, X. Wang, Deep learning-based detection for COVID-19 from chest CT using weak label, medRxiv.
[56] X. Xu, X. Jiang, C. Ma, P. Du, X. Li, S. Lv, L. Yu, Q. Ni, Y. Chen, J. Su, G. Lang, Y. Li, H. Zhao, J. Liu, K. Xu, L. Ruan, J. Sheng, Y. Qiu, W. Wu, T. Liang, L. Li, A deep learning system to screen novel coronavirus disease 2019 pneumonia, Engineering 6 (2020) 1122–1129.